Supplemental Information: Structural and Transport Properties of Battery Electrolytes at Sub-zero Temperatures

Nikhil Rampal[1,2,*], Stephen E. Weitzner[1,2,*], Seongkoo Cho[1,2], Christine A. Orme[1,2], Marcus A. Worsley[1,2], and Liwen F. Wan[1,2,*]

[1]Materials Science Division, Lawrence Livermore National Laboratory, Livermore, California, 94550, United States
[2]Laboratory for Energy Applications for the Future (LEAF), Lawrence Livermore National Laboratory, Livermore, California, 94550, United States
[*]rampal1@llnl.gov, weitzner1@llnl.gov, wan6@llnl.gov

Contents

S1 Classical Molecular Dynamics Simulations

Classical Molecular Dynamics (CMD) simulations were carried out using the LAMMPS[1] software package. To systematically assess the structural and transport properties, we consider $LiPF_6$/EC electrolyte concentrations between 0.2–5 M across a temperature range of 233–298 K (–40 – 25 °C). Initial configurations were generated for each electrolyte concentration by randomly placing ions and solvent molecules within a periodic simulation cell using Packmol[2]. All-atom optimized potentials for liquid simulations (OPLS-AA)[3–5] potentials were used to describe interatomic interactions within the system. To accurately treat ion transport behavior within our simulations, ion charges were scaled to 80 % of their original value[5]. To ensure the validity and accuracy of the force field, existing literature data for the density, viscosity, and diffusion coefficients was utilized as benchmarking data, shown in Fig. S2. The particle-particle particle-mesh solver (pppm)[6] was used for the long-range electrostatic force calculation with a threshold of 1×10^{-4}. The Nose-Hoover thermostat [7, 8] and the Parrinello-Rahman barostat[9] were utilized to maintain the temperature and pressure of the simulation. First, each system (at a specific electrolyte concentration) was equilibrated for 10 ns in an isothermal-isobaric (NPT) ensemble [10, 11] at 298 K and 1 bar to stabilize the solvent density. Then, the system was cooled down from 298 K to 233 K to obtain the electrolyte at various temperature intervals (298, 283, 273, 263, 253, 243 and 233 K), with a 2K/ns cooling rate. At each respective combination of temperature and concentration, a production run of 100 ns was conducted in NPT ensemble. All these simulations used a timestep of 1 femtosecond (fs). An example of the simulation box at 1 M and 298 K is shown in Fig. S1. Trajectory information was saved every 1000 steps (1 ps) for further analysis, from which both structural properties (density, radial distribution function, coordination number analysis, degree of clustering/ordering) and transport properties (diffusion coefficient, viscosity, ionic conductivity, and static dielectric constant, ion lifetimes) were calculated.

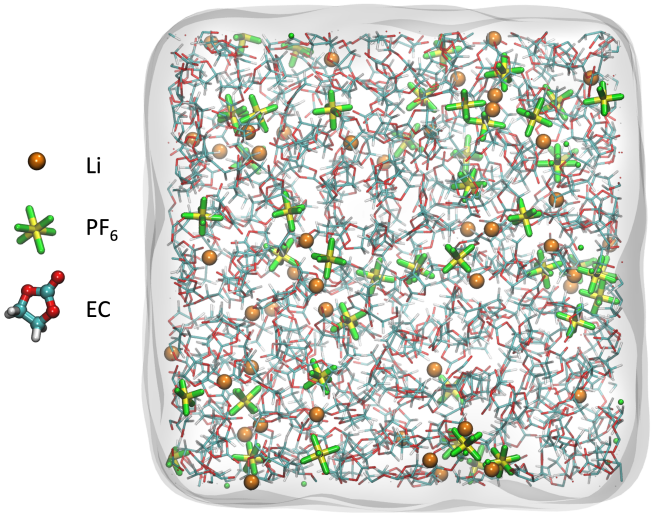

Figure S1: Snapshot of simulation box of 1 M $LiPF_6$ in Ethylene Carbonate (EC).

S1.1 Calculation of structural properties

To elucidate the structural properties of $LiPF_6$/EC electrolyte, radial distribution function, coordination numbers, and degree of clustering/ordering are calculated from CMD simulations. These properties were then deconvoluted into specific ion pairs to understand their fundamental atomic-level relationships. These structural properties were generated from VMD[12] and the PyLAT software[13]. The degree of clustering was calculated using a graph-based approach. To do this, a graph[14] is calculated at every step (1 ps) using the Li–P distance as the node cut-off and binned into a two-dimension function that contains the number of cations (Li) and anions(PF_6) that belong to the cluster. This Li-P distance was obtained from the first minima in the Li-P radial distribution function.

S1.2 Calculation of transport properties

The diffusion coefficient, viscosity, ionic conductivity, static dielectric constant, and ion lifetimes were calculated using an in-house code coupled with the PyLAT software[13]. Ion diffusion coefficients (D_{Li} and D_{PF_6}) were calculated based on mean square displacement (MSD) for each ion component. The diffusion coefficients ($D_{Cluster}$) of each cluster were calculated similarly, but instead of considering each ion, the center of mass of each cluster is considered as the frame of reference for the MSD calculation. In addition, the lifetimes of these clusters were calculated. To ensure that the fluctuations (cluster breaking and forming) were included, a 2 picosecond (ps) threshold was incorporated in the code. For example, if the cluster breaks and reforms within 2 ps timeframe, it is considered the same cluster along the respective trajectory. However, if the cluster breaks and doesn't reform within 2 ps, it is considered a new cluster/entity. The total ionic conductivity and its resolution into its specific contribution for different moieties were performed using the cluster Nernst-Einstein expansion [15]. In practice, the ionic conductivity is proportional to the diffusion coefficients of the ionic species, and in this formalism, one of the main assumptions is that the ions don't interact with each other. This approximation is valid for dilute systems; however, if the concentration of ionic species or the dielectric of the solvent is low, this assumption breaks down. Since we are interested in properties at low temperatures and high concentrations, we have utilized the recent cluster Nernst-Einstein equation, which considers clusters and not ions to correlate motion to ionic conductivity. This is imperative since we observe significant cluster formation, especially at high electrolyte concentrations.

S1.3 Benchmarking classical force field to existing literature data

The classical OPLS-AA force field was benchmarked to existing literature data. The properties that were used for this purpose were the density, transference numbers, viscosity, and diffusion coefficients. In Fig. S2(a), the force field is compared to computational estimates from Chaudhari *et al.*[16]. In Fig. S2(b), the transference numbers (t_+) were benchmarked to EIS, NMR and CMD data from Hayamizu *et al.*[17]. In Fig. S2(c), the viscosity is compared to EC/DMC (50:50wt%)[18]. In Fig. S2(d), diffusion coefficients from classical MD simulations compared to Porion *et al.*[18] and Hayamizu *et al.*[17]

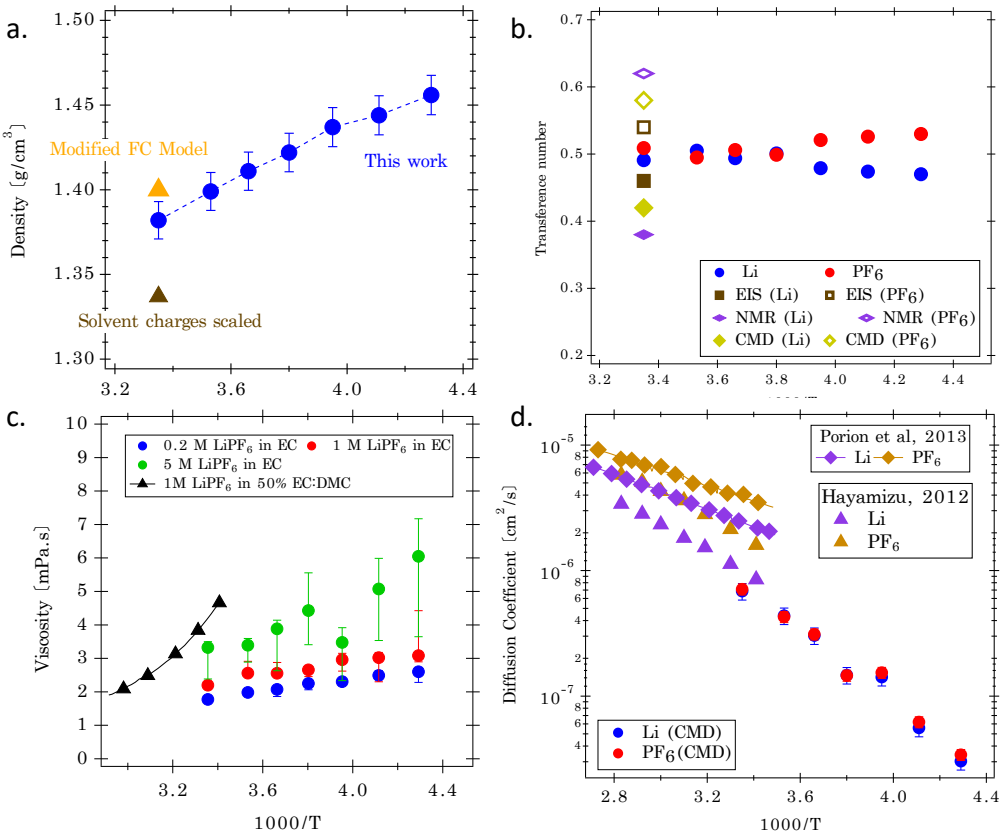

Figure S2: Various structural and transport properties obtained classical MD simulations are benchmarked to existing literature data. All the green, red and blue markers are data generated using the OPLS-AA force field used for this study. The properties benchmarked are: a) density, b) transference numbers, c) viscosity and d) diffusion coefficients

S2 Diffusivity parameters

The calculated activation barriers associated with Li-ion diffusion are presented in Table S1. As the concentration increases, the activation barriers (E_A) also increase, starting from 0.29 eV at 0.2 M to 0.52 eV at 1 M concentration. An inflection point is observed at 1 M, beyond which the activation barriers start to decrease.

Table S1: Diffusivity parameters derived from Arrhenius model fits to CMD-derived diffusivity data for $LiPF_6$/EC electrolytes across a temperature range of −40 to 25 °C.

Concentration [M]	Prefactor, D_0 [$cm^2\ s^{-1}$]	Activation Energy, E_A [eV]
0.2	0.23	0.29
0.4	0.12	0.29
0.5	0.31	0.32
1	1028.00	0.52
2	6.09	0.43
3	0.59	0.40
4	1.50×10^{-3}	0.28
5	6.00×10^{-4}	0.26

S3 Double peak in Li-P radial distribution function

The double Li – P peak in the radial distribution arises from different coordination environments that changes with respect to concentration. At low salt concentrations, there are multiple conformations that can be observed, that is, conformation 1: 80° and 148° at 3 Å and conformation 2: 110° at 3.9 Å. The first confirmation is a bidentate site with the Li-ion partially bonded to two F(PF_6). The second confirmation is the monodentate site, with the Li bonded to just one F and therefore the corresponding Li – P bond length is slightly further away (at 3.9 Å). As the concentration increases, the probability frequency of the first confirmation, or the bidentate site decreases, and the predominant state is the monodentate site. This is because as the solute concentration increases, the effect of steric hindrance is much more pronounced, thereby constraining the ions into specific localized geometries.

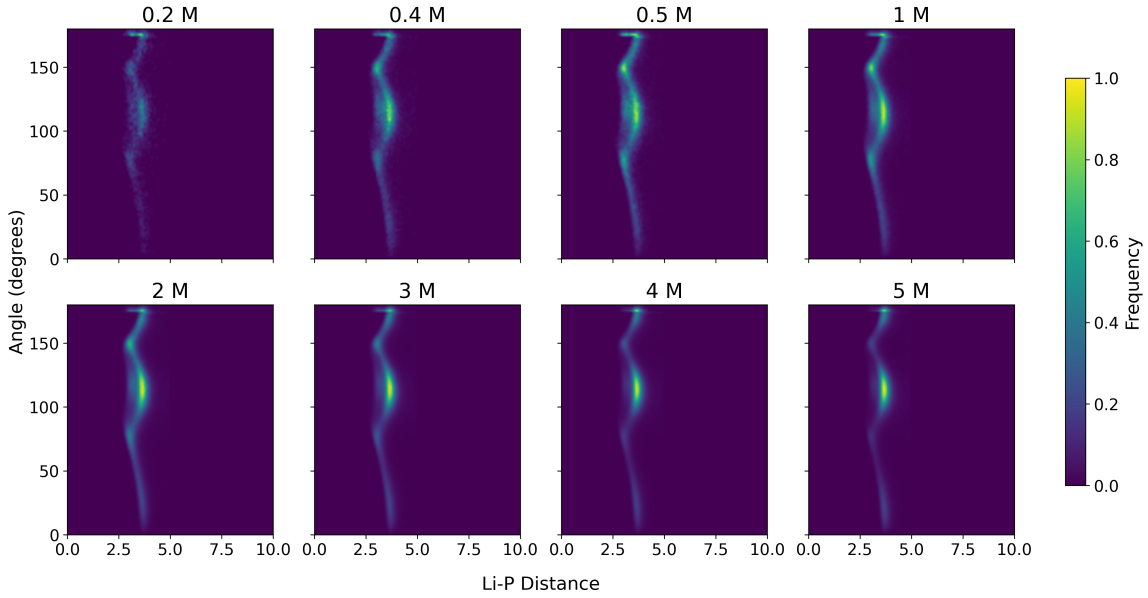

Figure S3: The normalized frequency of the angle formed by the ∠Li–F–P as the Li – P distance varies. The subplots show the concentration dependence the color bar represents the normalized frequency.

S4 Diffusion coefficients (D_{ij}) of clusters observed in $LiPF_6$/EC electrolyte

The diffusion coefficients (D_{ij}) of each cluster observed in the electrolyte over the concentration range (0.2 to 5 M) at 298.15 K is shown below in Fig. S4. The orange, red, blue and green makers represent $N_{Cluster} = 1$, neutral ($N_{cation} = N_{anion}$), positive ($N_{cation} > N_{anion}$) and negative ($N_{cation} < N_{anion}$) clusters. These coefficients span a wide range, from 10^{-9} m^2/s to 10^{-13} m^2/s, which is close to four orders of magnitude shift with variations in concentration. A consistent trend emerges, wherein an increase in electrolyte concentration corresponds to a increase in cluster formation, and therefore a corresponding decrease in D_{ij}. This observed pattern in diffusion coefficients can be attributed to the heightened propensity for cluster formation at elevated electrolyte concentrations, particularly beyond saturation limit (1.72 M). Beyond the saturation limit, we observe the onset of particle nucleation, represented by large clusters being formed. At 5 M concentration, we observe a phase transition (clusters with $n_{species} > 350$).

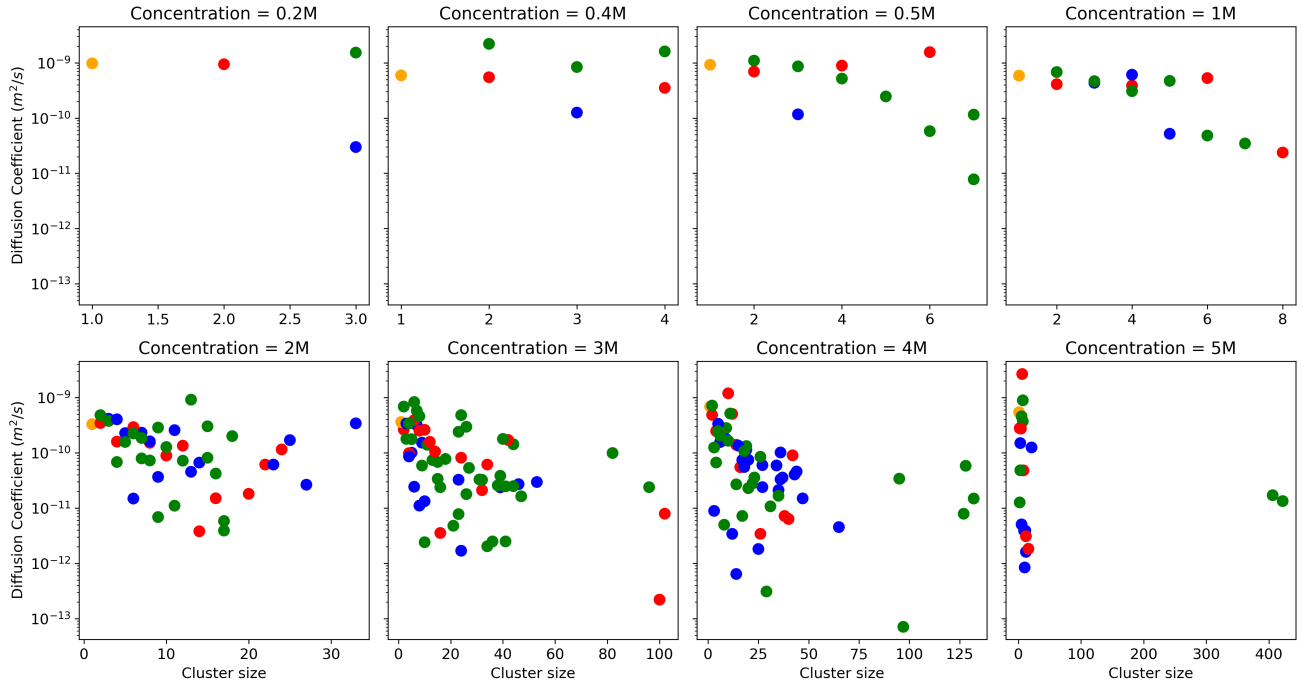

Figure S4: The diffusion coefficient for each cluster size over the concentration range at 298.15 K. The orange, red, blue and green makers represent $N_{Cluster} = 1$, neutral ($N_{cation} = N_{anion}$), positive ($N_{cation} > N_{anion}$) and negative ($N_{cation} < N_{anion}$) clusters.

S5 Cluster population analysis observed in $LiPF_6$/EC electrolyte

The composition of the electrolyte in terms of distribution of various types of moieties, the concentration-dependent cluster population (μ_{ij}, where i and j is the number of cations and anions in the respective cluster) at 298.15 K. At 0.2 M concentration, the electrolyte is primarily composed of fully solvated Li (μ_{10}) and PF_6(μ_{01}) ions with minor occurrences of $LiPF_6$ (μ_{11}) ion pairs, $Li(PF_6)_2$ (μ_{12}) and Li_2PF_6 (μ_{21}) trimers. With the increase in electrolyte concentration, the propensity to form larger clusters also increases. At 0.4 M concentration, in addition to the fully solvated ions and ion-pairs, larger moieties, such as $Li_2(PF_6)_2$ (μ_{22})and $Li(PF_6)_3$ (μ_{13}) tetramers and even a small frequency of pentamers (μ_{32} and μ_{23}) and hexamers (μ_{33} and μ_{24}). At 1 M concentration, considerable variation of cluster sizes is observed in the simulation, ranging from fully solvated ions (μ_{10} and μ_{01}) to hexamers ($\mu_{i+j=6}$) , octamers ($\mu_{i+j=8}$), decamers ($\mu_{i+j=10}$) and so forth. A noteworthy observation is that with increasing concentration, we witness a noticeable shift/asymmetry in the clusters observed (dashed yellow line) from the neutral clusters (solid red line), which implies that these clusters tend to be negatively charged, i.e. $n_{anions} > n_{cations}$ ($\mu_{i<j}$). These findings also hold for concentrations beyond 1 M, with limited presence of positively charged free ions, ion pairs and smaller-sized clusters, and predominately negatively charged larger clusters. Negatively charged clusters like those exhibited in this system can significantly impact overall battery performance by dictating electrolyte conductivity, altering the structure and chemistry of electrode-electrolyte interfaces, and influencing its chemical, thermal stability and safety and thus it is imperative to understand how these cluster are formed, under what condition and to what degree it affect the transport properties of the electrolyte.

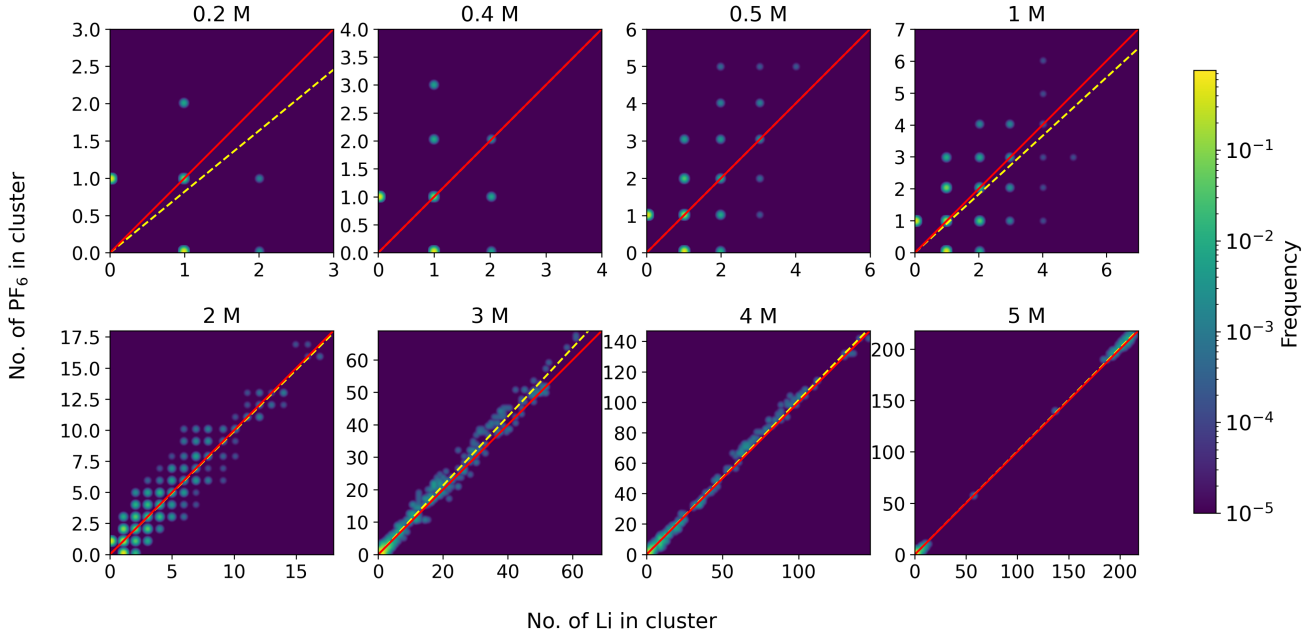

Figure S5: Cluster size distribution of types of moieties, the concentration-dependent cluster population (μ_{ij}, where i and j is the number of cations (*x-axis*) and anions (*y-axis*) in the respective cluster). The red line represented neutral clusters and the yellow line depicts the shift in cluster observations. The frequency of each cluster is shown by the color scale on the right.

S6 Temperature-dependent speciation observed in $LiPF_6$/EC electrolyte

The temperature-dependent ionic speciation across the electrolyte concentration is shown in Fig. S6. At low concentrations ($<$ 1 M), the electrolyte comprises of solvated ions (Li^+ and PF_6^-, SSIP and SSHIP) and ion pairs (Li-PF_6). This remains consistent, even at low temperatures ($<$ 283 K). As the concentration exceeds the saturation index (1.72 M), larger aggregates (hexamers, septamers, and so on) are observed. Similar to the trends observed at low concentrations, the ionic speciation consistently remains the same at low temperatures. This signifies that the temperature of the electrolyte may not be a key driver in ionic speciation.

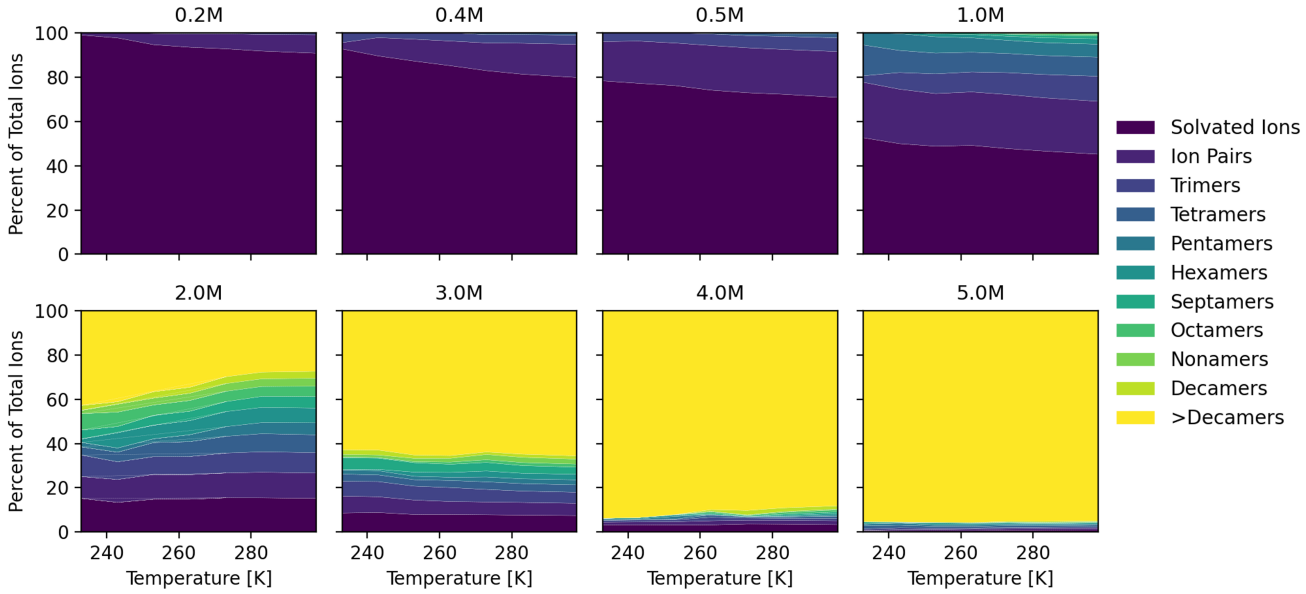

Figure S6: Temperature dependent speciation in $LiPF_6$/EC electrolyte. The colors represent the type of ionic species observed in the electrolyte.

S7 Transference numbers (t_+) as a function of temperature (K) and concentration (M)

Transference numbers (t_+) for $LiPF_6$ in EC are calculated using the Nernst-Einstein (t_+^{NE} and its variant cluster-Nernst-Einstein (t_+^{cNE}) expression[15]. Details of the implementation is in Section S1. Briefly, the t_+^{NE} always yields values greater than 0, shown by the open markers in Fig. S7. This means that there is always a positive correlation of the anion and/or cation to overall conductivity. However, using the cluster-Nernst-Einstein expression can yield $t_+^{cNE} < 0$. There is experimental evidence of this, as described in the main text. At low concentrations (< 1 M), both the t_+^{NE} and t_+^{cNE} have similar values. Whereas, at high concentrations (> 3 M), where ion aggregation and clustering becomes significant, the t_+^{cNE} diverges, where we start to observe negative values ($t_+^{cNE} < 0$). This is especially evident at high concentrations and low temperatures. The origins of negative values are due to the negatively-charged aggregates that form at high concentrations and low temperatures, resulting in negative electrophoretic mobility.

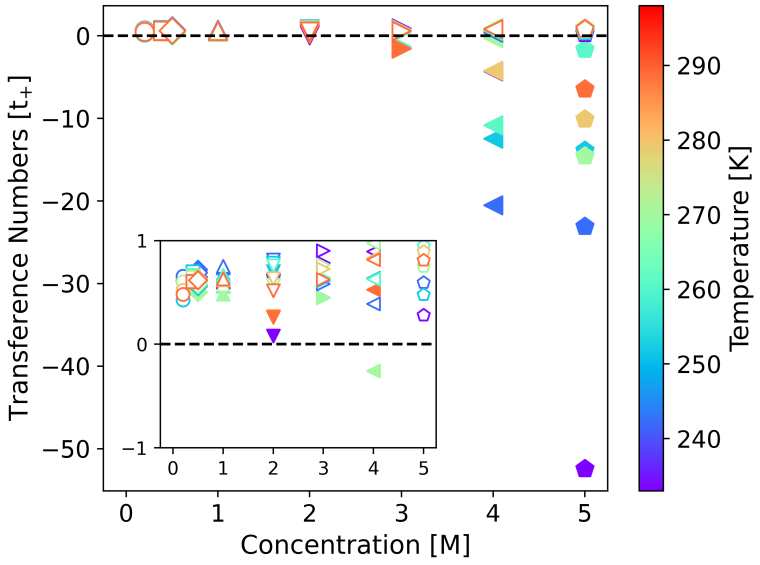

Figure S7: Transference numbers (t_+) of Li-ion (*x-axis*) as a fucntion of the electrolyte concentration (M). The temperature of the electrolyte is distinguished by the marker colors, shown by the colorscale. The solid markers are t_+^{cNE} obtained from Cluster Nernst-Einstein Equation and open makers are t_+^{NE} obtained from Nernst-Einstein Equation. The inset is zoomed to shown the range of t_+ = [-1,1]

S8 Diffusion coefficients (D_{Li}) of lithium ions in SSIP, SSHIP and CIP observed in $LiPF_6$/EC electrolyte

The diffusion coefficients (D_{Li}) of lithium ions in solvent separated ion pairs (SSIP), solvent-shared ion pairs (SSHIP) and contact ion pairs (CIP), over the temperature (233 - 298 K) and concentration range (0.2 - 5 M). At low concentrations, the diffusion coefficients of these species are pretty similar. However, as the concentration goes beyond 2 M, the general observation is that the the SSIPs diffuse slower through the bulk electrolyte than the SSHIP and SIP. This is largely due to the size of the SSIP, which contains fully coordinated solvent (EC) molecules in its solvation shell. In addition, it is apparent from Fig. S8 is that as the temperature increases, there is an increase in diffusivity of lithium ions in SSIP, SSHIP and CIP.

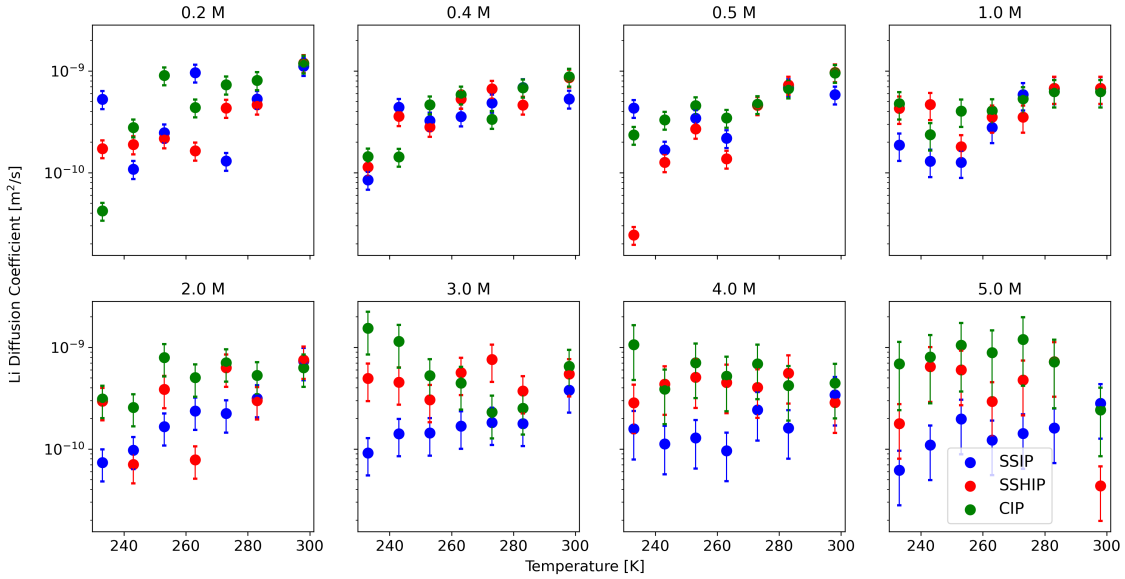

Figure S8: The diffusion coefficient of lithium ions (D_{Li}) in SSIP (blue), SSHIP (red) and CIP (green) over the concentration range (0.2 to 5 M) at 298 K.

S9 Concentration of Free Ions and Contact Ion pairs in $LiPF_6$/EC electrolyte

The temperature dependence of the concentration (M) of Free ions (SSIPs + SSHIPs) and Contact Ion Pairs (CIP) is mapped over the concentration range (0.2 to 5 M), and is depicted in Fig. S9. The concentration of Free ions and CIPs increases with electrolyte concentration. There is an inflection point at 1 M concentration, where the concentration of Free ions and CIPs starts decrease. The temperature of the electrolyte does not play in significant role in the concentration of Free ions and CIPs, as it tends to remain the same, even at low temperatures. This is also shown in Fig. S6 in Section S6.

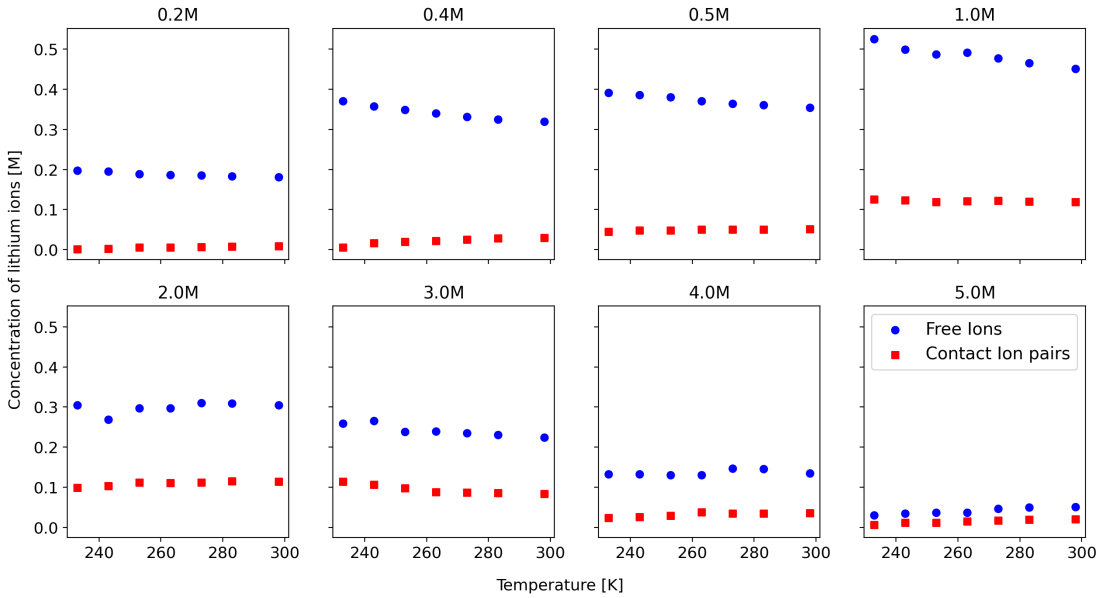

Figure S9: Concentration of free ions (blue), and contact ion pairs (red) over the temperature (233 to 298 K) and concentration range (0.2 to 5 M)

S10 Diffusion coefficients of Ethylene Carbonate in $LiPF_6$/EC electrolyte

The diffusion coefficients of Ethylene Carbonate (EC) were calculated using the Nernst-Einstein Equation (details in Section S1). As expected, we observe that the EC diffusion coefficient decreases with decreasing temperature at each electrolyte composition. The rate at which the diffusion coefficient decreases is fit to an Arrhenius relation

$$\ln D = \ln D_0 - \frac{E_A}{k_B T}, \tag{S1}$$

and the extracted effective activation energies E_A for EC diffusion are summarized in Table S2.

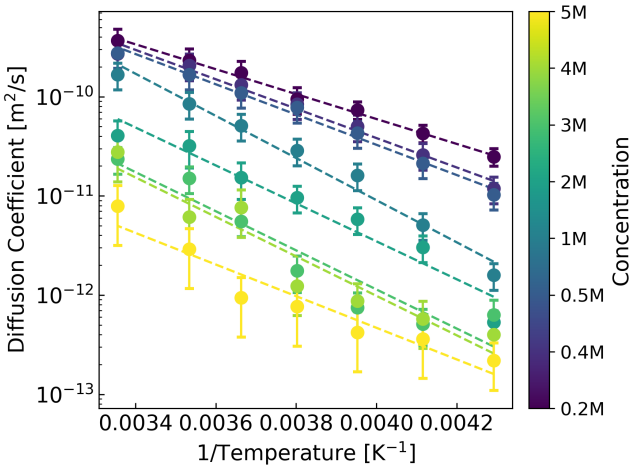

Figure S10: Diffusion coefficients (m^2/s) of Ethylene Carbonate in bulk $LiPF_6$ in EC electrolyte as a function of inverse temperature (K^{-1}), obtained from Classical MD simulations. The marker colors represent the concentration (M) of the electrolyte, shown by the colorscale on the right.

The activation energy (E_A) can serve as a useful descriptor for the degree to which the EC diffusivity is suppressed at lower temperatures (Similar to Fig 1). The activation energy (E_A) increases as the concentration of the electrolyte increases. It reaches an inflection point at 1 M concentration and then starts to decrease (E_A = 0.28 eV at 5 M). Therefore, at 1 M concentration, we observe the largest change in EC diffusion from 298 to 233 K, represented by the largest E_A = 0.42 eV.

Table S2: Ethylene carbonate (EC) diffusivity parameters derived from Arrhenius model fits to CMD-derived diffusivity data for $LiPF_6$/EC electrolytes across a temperature range of −40 to 25 °C.

Concentration [M]	Activation Energy, E_A [eV]
0.2	0.25
0.4	0.29
0.5	0.30
1	0.42
2	0.41
3	0.41
4	0.38
5	0.28

S11 Ethylene carbonate (EC) lifetimes around the Li-ion

The EC lifetimes around the Li-ion were calculated using the PyLAT software[13]. These lifetimes monitor the average time (in ps) the EC molecule spends in the Li-ion solvation shell. These lifetimes are plotted as a function of inverse temperature and shown below in Fig. S11. We observe as the temperature increases from 233 to 298 K, the average lifetimes of EC decreases. The extracted activation energies (E_A) are shown in Table S3.

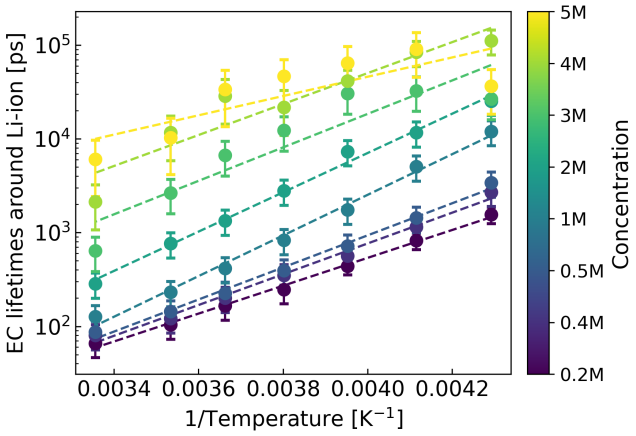

Figure S11: Lifetimes of Ethylene carbonate (EC) around the Li-ion (in ps) as a function of inverse temperature (K^{-1}).The marker colors are representing the concentration (M) of the electrolyte, shown in the legend

We observe a similar trend in E_A of EC lifetimes to the E_A of EC diffusion. As the concentration increases, the activation energy also increases. It reaches an inflection point at 1 M concentration (E_A= 0.42 eV) and then starts to decrease. Therefore the largest change in EC lifetimes around the Li-ion is at 1 M concentration. In the following section, we elucidate the correlation between the activation barriers of these various processes (Li diffusion, EC diffusion and EC lifetimes).

Table S3: Ethylene carbonate (EC) lifetimes derived from Arrhenius model fits to CMD-derived lifetime data for $LiPF_6$/EC electrolytes across a temperature range of −40 to 25 °C.

Concentration [M]	Activation Energy, E_A [eV]
0.2	0.29
0.4	0.32
0.5	0.34
1	0.43
2	0.41
3	0.36
4	0.33
5	0.20

S12 Correlation of Activation barriers (E_A) of Li-ion Diffusion to the E_A of EC Diffusion and E_A of EC lifetimes around the Li-ion

To explain the large temperature-dependent drop in Li-ion diffusivity (shown by large E_A value in Table S1) at 1 M concentration, the activation barriers associated with solvent (EC) diffusion and solvent lifetimes within the Li-ion solvation shell are correlated to Li-ion diffusion, in Fig. S12(a) and Fig. S12(b). There is a distinct correlation with both EC diffusion and EC lifetimes to Li-ion diffusion, that is, the E_A exhibits the largest change over the temperature range at 1 M. Therefore, we can conclude that the large drop in Li-ion diffusivity can be attributed to the solvent diffusion and lifetime.

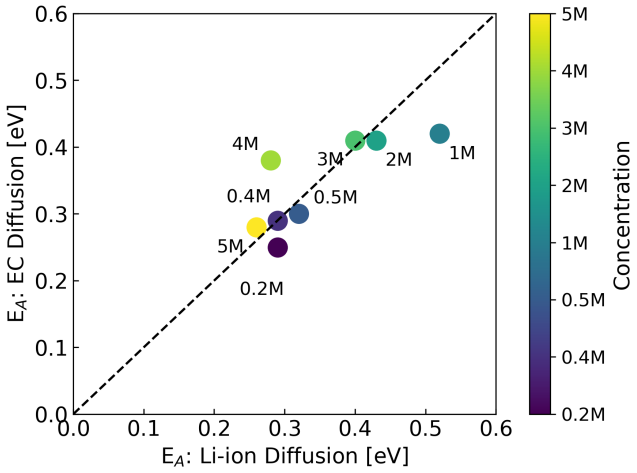

(a)

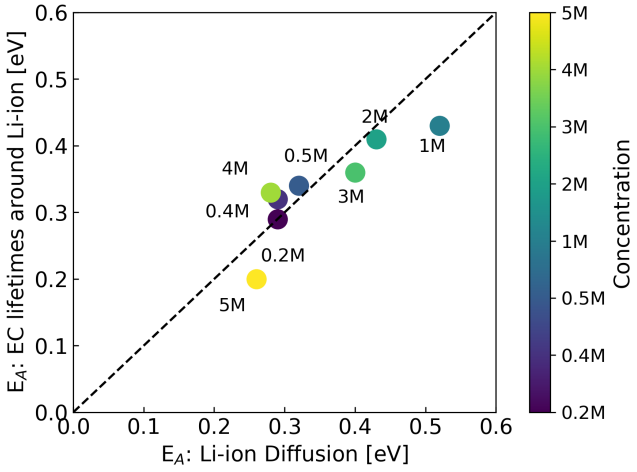

(b)

Figure S12: Correlation of the Activation Barriers (E_A) of Li-ion diffusion to (a) EC diffusion and (b) EC lifetimes around the Li-ion solvation shell. The parity line is represented by dashed line. The concentration (M) of the electrolyte is distinguished by the marker colors, shown by the color scale.

S13 Viscosity (η) and Molar Conductivity (Λ_m) of $LiPF_6$ in Ethylene Carbonate

The viscosity (η) of the electrolyte is investigated as a potential descriptor for low-temperature performance. The changes in η as a function of concentration (M) and temperature (K) are shown in Fig. S13. As the concentration increases, the viscosity of the electrolyte increases. This is due to the formation of larger-sized clusters/aggregates in the electrolyte, leading to slower Li-ion diffusion, and therefore, making the electrolyte much more viscous. Concurrently, as the temperature decreases, the viscosity tends to also decrease. This is due to the hindered diffusion at such low temperatures (< 260 K).

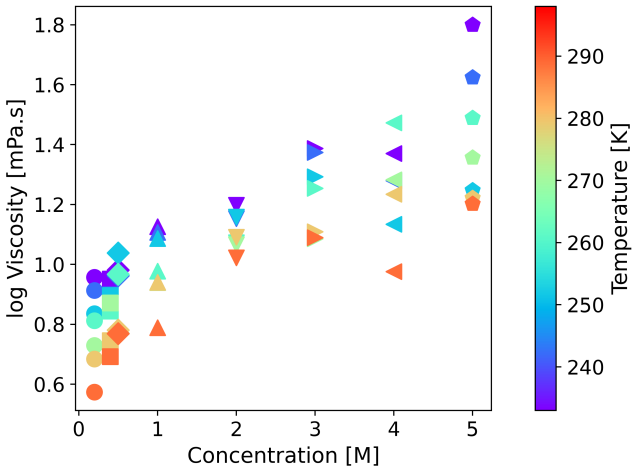

Figure S13: The change in electrolyte viscosity (η) as a function of concentration and temperature. The temperature (K) is represented by the color scale on the right.

We correlate the η descriptor to the a metric that represents overall electrolyte performance, that is the molar conductivity (Λ_m). Combining the Stokes-Einstein with the Nernst-Einstein equation yields the Walden rule that states that the product of molar conductivity and viscosity is constant, as shown by the equation below.

$$\Lambda_m \cdot \eta = constant \tag{S2}$$

In the system studied here, it is evident the the product (shown in Eq. S2) is not constant across the concentration and temperature range (Fig. S14(a)). From this relationship, we can deduce that much more complex solute-solvent interactions are responsible for this non-linearity. This is likely due to the complex ionic speciation in the electrolyte, shown in Figure S14(b). The parity line represents a fully dissociated electrolyte where the mobility of the ionic species are equal[19]. We observe a linear trend that diverges from the parity line. This divergence is much more prominent at low temperatures and at high concentrations. This can be explained by the coupling effect of the degree of ionic speciation and slower ion mobility in such environments. This is particularly important because this is representative of electrolytes that will be observed in extreme environments, and understanding the coupling of these metrics can provide rationale to design more robust battery electrolytes.

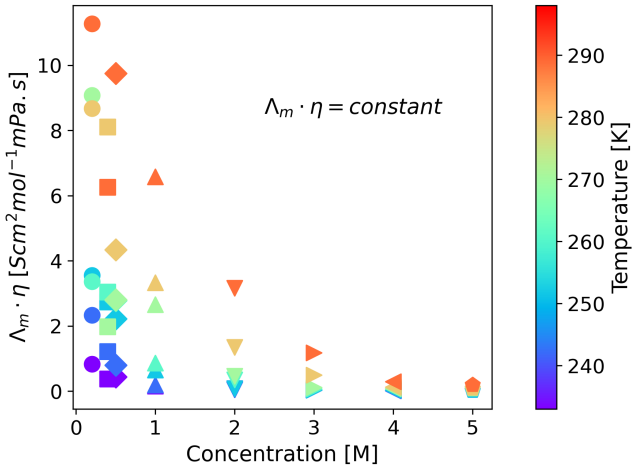

(a)

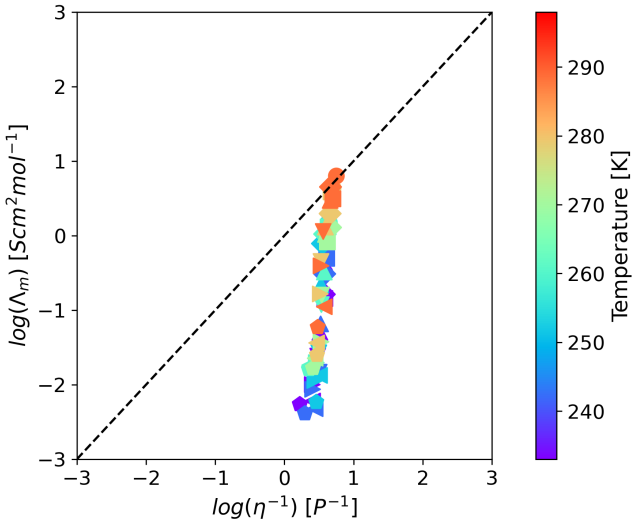

(b)

Figure S14: Correlation of the molar conductivity (Λ_m), viscosity (η) with concentration (M) and temperature (K). (a) Non-linear change of product of Molar conductivity and Viscosity as a function of electrolyte concentration and (b) Walden plot showing the parity (black dotted line) of the viscosity and the molar conductivity of $LiPF_6$ in EC electrolyte. The temperature (K) is represented by the color scale on the right.

S14 Experimental Methodology

The experiment for measuring ionic conductivity was conducted using a simple two-electrode system, as depicted in Fig. S15(a). The setup involved a cylindrical electrolyte volume with a diameter of 5 mm and an electrode spacing of 5 mm. The electrodes used were thin-film gold electrodes plated on glass substrates. The two-electrode cell was subsequently transferred to the thermal chamber, where its conductivity was measured at a temperature range spanning from room temperature to -30°C, with changes of approximately 10°C every 12 minutes, following the completion of sealing operations performed within an argon glovebox. Ionic conductivity was calculated from measurements obtained using Electrochemical Impedance Spectroscopy (EIS), as shown in Figure S15(b). Electrochemical measurements were performed as a set by first measuring the open-circuit potential (OCP) for 10 seconds, followed by EIS measurements. This process was continuously repeated as the temperature was adjusted. The EIS was conducted at an amplitude of 10 mV, with a frequency range from 100 kHz to 10 Hz, recording 10 points per decade. As illustrated in the electrical equivalent model in Fig. S15(b), the ionic conductivity was calculated by first obtaining the solution resistance from the real part of the impedance at high frequency. The temperature-dependent ohmic resistance due to each gold electrode line was subtracted from this value. The ohmic resistance value from gold electrode was calculated measuring a well-known electrical conductivity of 0.1 M NaCl solution[20], with a temperature coefficient of 0.0034 K^1[21], across a temperature range from room temperature to 5°C. The final ionic conductivity is obtained by dividing the geometric factor ($k = l/A \cong 2.55$) by the corrected resistance[22]

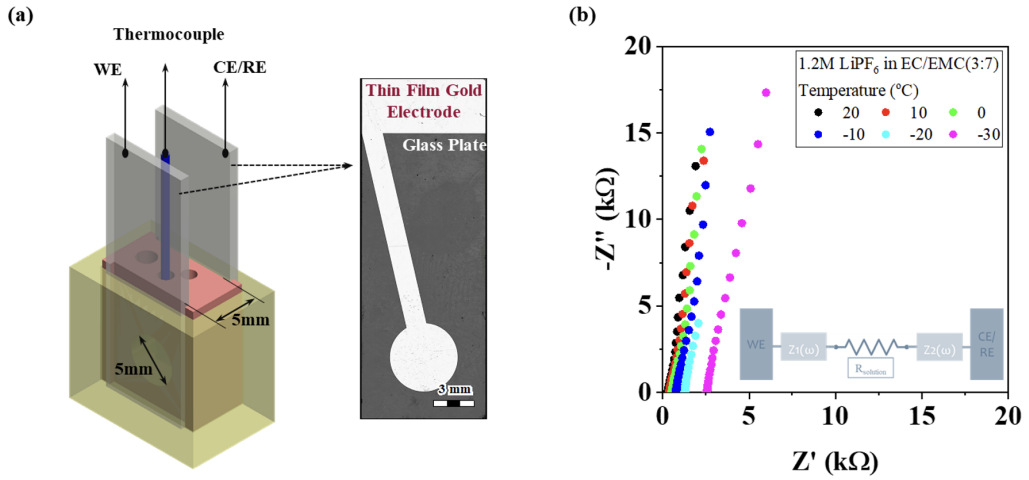

Figure S15: (a) Schematic design of a two-electrode note cell used for measuring ionic conductivity. (b) Nyquist plots obtained from impedance measurements using the two-electrode system at various temperatures, along with the corresponding impedance equivalent circuit model.

S15 Comparing ionic conductivity

The ionic conductivity was measured using EIS experiments (Section S14) and computational simulations, shown in Fig. S16. Performing a one-to-one quantitative comparison is not feasible since the OPLS-AA [3–5] classical force field used here is benchmarked to experimental transport properties, that is, the Li-ion diffusion. Also, the ionic conductivity is sensitive to the method used: Nernst-Einstein, cluster Nernst-Einstein or Green-Kubo Method. Therefore to remove this 'bias', we scale the conductivity to the minimum value, thereby, normalizing each observation. In addition, classical force fields *as-is* tend to underestimate the ionic conductivity (shown in Fig. S16). This uncertainty in the computed ionic conductivity using classical force fields is well documented in literature[23–25], and correcting the force field parameters to reflect the experimental measurements[26, 27] accurately requires modifications and adding further complexities to the force field, such as including parameters that include polarization effects. Nonetheless, the trends shown below are within reasonable error, validating our potential for some benchmarked properties.

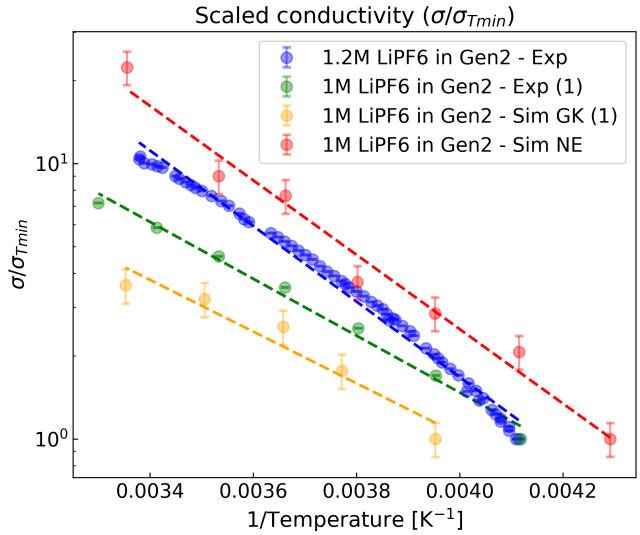

Figure S16: (a) Experimental conductivity measurements (in blue) as a function of inverse temperature. Green and yellow datapoints correspond to experimental and simulation data from Ringsby et al [24].

S16 Extension of design principles to 1 M $LiPF_6$ in EC:EMC (3:7)

The first design principle for improving room temperature performance emphasizes maximizing the number of highly mobile charge carriers. In the figure below, we show a side-by-side comparison of the number of mobile charge carriers for 1 M $LiPF_6$ in EC and in EC: EMC. We observe a similar trend with the mixed EC:EMC electrolyte as we do in the pure EC electrolyte, where the number of mobile charge carries is maximized around a concentration of 1.0M. And as shown throughout our study and in literature, maximizing the number of mobile charge carriers is a key factor for maximizing the ionic conductivity. The computational estimates for the ionic conductivity are 2.8 (0.5 M), 3.15(1 M), and 2.03(2 M) mS/cm. This parabolic trend in conductivity has previously been observed for the same electrolyte in experiments[28]).

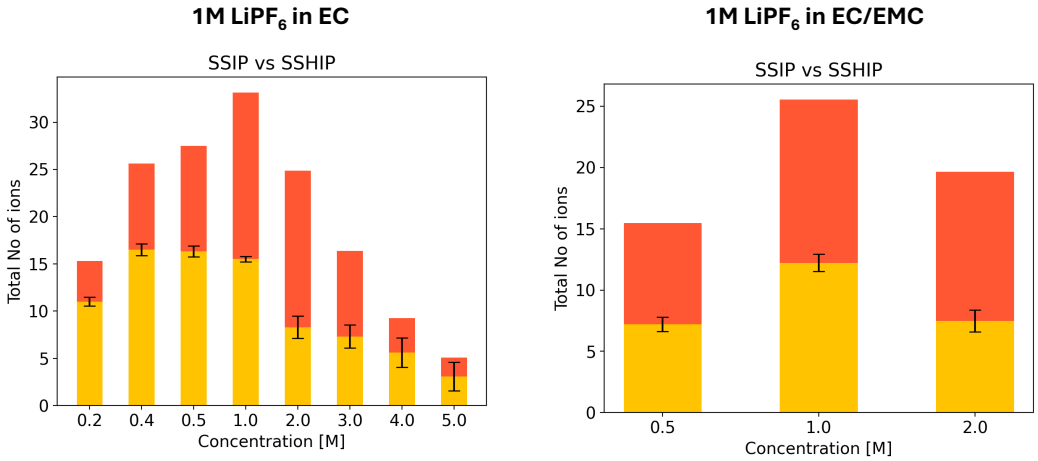

Figure S17: The total number of solvent-separated ion pairs (SSIPs) and solvent-shared ion pairs (SSHIPs), as a function of concentration at 298 K for 1 M $LiPF_6$ in EC (left) and 1 M $LiPF_6$ in EC:EMC (right).

The second design principle states that solvent transport and electrolyte viscosity govern the performance of the electrolyte at low temperatures. While our laboratory was unable to provide temperature-dependent viscosity data in support of this manuscript, some data does exist in the literature. For a recent example, Ringsby et al. [24] report temperature-dependent viscosity data for 1 M $LiPF_6$ in EC:EMC that was measured using an electromagnetically spinning viscometer. One of the key conclusions they drew from their findings was that "the dominant factor influencing low-temperature transport is solvent viscosity, rather than ion aggregation or cation transference number," which offers strong support for our second design principle.

From these two observations, we believe that our theoretical temperature-dependent physicochemical properties derived from the simplified model can have a credible impact on formulating design strategies for realistic battery electrolytes such as the 1 M $LiPF_6$ EC:EMC electrolyte considered above.

S17 Mode of transport in $LiPF_6$/EC electrolyte

To distinguish the type of diffusion in $LiPF_6$ in EC, we use the methodology shown in Self et al. [29] to decipher the mode of diffusion as vehicular, structural, or mixed within the electrolyte. This is done with the characteristic length (L^C):

$$L_{ij}^{c} = \sqrt{6 D_{ij} \tau_{ij}^{res}} \tag{S3}$$

$if\ L_{ij}^{c} > L^{S} \rightarrow\ vehicular\ diffusion$
$if\ L_{ij}^{c} < L^{S} \rightarrow\ structural\ diffusion$

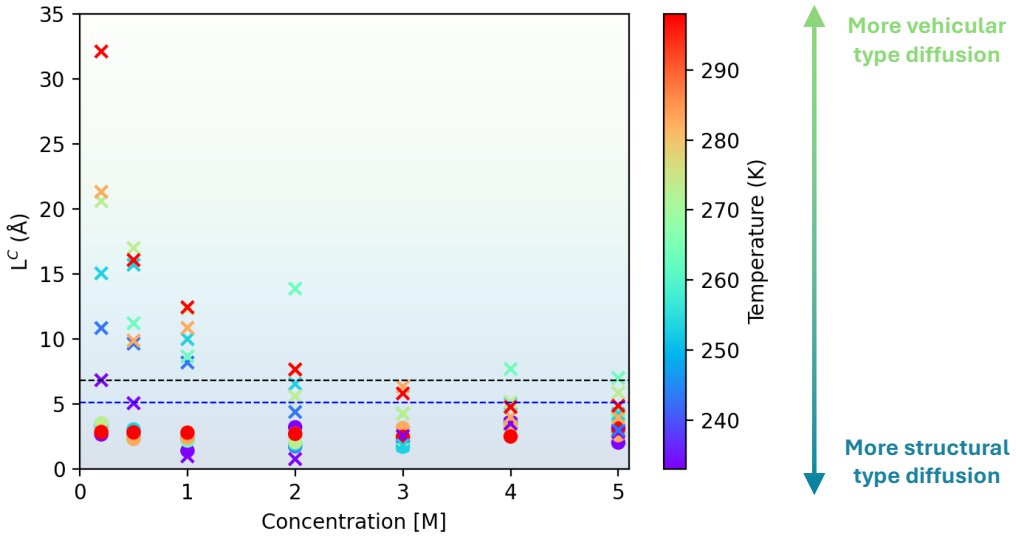

Figure S18: Characteristic length (L^C) as a function of concentration (x-axis) and temperature (color scale). The circle and cross markers represent L^C(Li-EC) and L^C(Li-PF_6). The black and blue dashed lines are L^S (Li-EC) = 6.8 and L^S (Li-PF6) = 5.1

The value of solvation shell (L^S) is extracted from the minima in the radial distribution function. The values are L^S (Li-EC) = 6.8 and L^S (Li-PF_6) = 5.1. The Li diffusion mode with respect to EC (L^C (Li-EC)), shown by the circle markers, is generally less than 5; therefore, it represents structure-type diffusion, even at high concentrations. Meanwhile, the diffusion mode with respect to PF_6 (L^C (Li-PF_6)) changes drastically with respect to concentrations. The transport mechanism is more vehicular at low concentrations (< 2 M). As the concentration increases, L^C decreases, trending towards more mixed (diffusion + structural) and, finally, structural mode is diffusion type at 5 M concentration.

References

1. Thompson, A. P. *et al.* LAMMPS-a flexible simulation tool for particle-based materials modeling at the atomic, meso, and continuum scales. *Computer Physics Communications* **271,** 108171 (2022).
2. Martínez, L., Andrade, R., Birgin, E. G. & Martínez, J. M. PACKMOL: A package for building initial configurations for molecular dynamics simulations. *Journal of computational chemistry* **30,** 2157–2164 (2009).
3. Jorgensen, W. L., Maxwell, D. S. & Tirado-Rives, J. Development and testing of the OPLS all-atom force field on conformational energetics and properties of organic liquids. *Journal of the American Chemical Society* **118,** 11225–11236 (1996).
4. Sambasivarao, S. V. & Acevedo, O. Development of OPLS-AA force field parameters for 68 unique ionic liquids. *Journal of chemical theory and computation* **5,** 1038–1050 (2009).
5. Doherty, B., Zhong, X., Gathiaka, S., Li, B. & Acevedo, O. Revisiting OPLS force field parameters for ionic liquid simulations. *Journal of chemical theory and computation* **13,** 6131–6145 (2017).
6. Hockney, R. W. & Eastwood, J. W. *Computer simulation using particles* (crc Press, 2021).
7. Nosé, S. A unified formulation of the constant temperature molecular dynamics methods. *The Journal of chemical physics* **81,** 511–519 (1984).
8. Hoover, W. G. Canonical dynamics: Equilibrium phase-space distributions. *Physical review A* **31,** 1695 (1985).
9. Parrinello, M. & Rahman, A. Polymorphic transitions in single crystals: A new molecular dynamics method. *Journal of Applied physics* **52,** 7182–7190 (1981).
10. Shinoda, W., Shiga, M. & Mikami, M. Rapid estimation of elastic constants by molecular dynamics simulation under constant stress. *Physical Review B* **69,** 134103 (2004).
11. Martyna, G. J., Tobias, D. J. & Klein, M. L. Constant pressure molecular dynamics algorithms. *The Journal of chemical physics* **101,** 4177–4189 (1994).
12. Humphrey, W., Dalke, A. & Schulten, K. VMD: visual molecular dynamics. *Journal of molecular graphics* **14,** 33–38 (1996).
13. Humbert, M. T., Zhang, Y. & Maginn, E. J. PyLAT: Python LAMMPS analysis tools. *Journal of chemical information and modeling* **59,** 1301–1305 (2019).
14. Hagberg, A., Swart, P. & S Chult, D. *Exploring network structure, dynamics, and function using NetworkX* tech. rep. (Los Alamos National Lab.(LANL), Los Alamos, NM (United States), 2008).
15. France-Lanord, A. & Grossman, J. C. Correlations from ion pairing and the Nernst-Einstein equation. *Physical review letters* **122,** 136001 (2019).
16. Chaudhari, M. I. *et al.* Scaling atomic partial charges of carbonate solvents for lithium ion solvation and diffusion. *Journal of chemical theory and computation* **12,** 5709–5718 (2016).
17. Hayamizu, K. Temperature dependence of self-diffusion coefficients of ions and solvents in ethylene carbonate, propylene carbonate, and diethyl carbonate single solutions and ethylene carbonate+ diethyl carbonate binary solutions of LiPF6 studied by NMR. *Journal of Chemical & Engineering Data* **57,** 2012–2017 (2012).
18. Porion, P. *et al.* Comparative study on transport properties for LiFAP and LiPF6 in alkyl-carbonates as electrolytes through conductivity, viscosity and NMR self-diffusion measurements. *Electrochimica Acta* **114,** 95–104 (2013).
19. Xu, W. & Angell, C. A. Solvent-free electrolytes with aqueous solution-like conductivities. *Science* **302,** 422–425 (2003).
20. McCleskey, R. B. Electrical conductivity of electrolytes found in natural waters from (5 to 90) C. *Journal of Chemical & Engineering Data* **56,** 317–327 (2011).
21. Le Bourdais, D. *et al.* Epitaxial manganite freestanding bridges for low power pressure sensors. *Journal of Applied Physics* **118** (2015).
22. Landesfeind, J. & Gasteiger, H. A. Temperature and concentration dependence of the ionic transport properties of lithium-ion battery electrolytes. *Journal of The Electrochemical Society* **166,** A3079–A3097 (2019).

23. Hou, T., Fong, K. D., Wang, J. & Persson, K. A. The solvation structure, transport properties and reduction behavior of carbonate-based electrolytes of lithium-ion batteries. *Chemical science* **12,** 14740–14751 (2021).

24. Ringsby, A. J. *et al.* Transport phenomena in low temperature lithium-ion battery electrolytes. *Journal of the Electrochemical Society* **168,** 080501 (2021).

25. Molinari, N., Mailoa, J. P. & Kozinsky, B. Effect of salt concentration on ion clustering and transport in polymer solid electrolytes: a molecular dynamics study of PEO–LiTFSI. *Chemistry of Materials* **30,** 6298–6306 (2018).

26. Biriukov, D. *et al.* The "good," the "bad," and the "hidden" in neutron scattering and molecular dynamics of ionic aqueous solutions. *The Journal of Chemical Physics* **156** (2022).

27. Rampal, N. *et al.* Local molecular environment drives speciation and reactivity of ion complexes in concentrated salt solution. *Journal of Molecular Liquids* **340,** 116898 (2021).

28. Logan, E. *et al.* A study of the physical properties of Li-ion battery electrolytes containing esters. *Journal of The Electrochemical Society* **165,** A21 (2018).

29. Self, J., Fong, K. D. & Persson, K. A. Transport in superconcentrated LiPF6 and LiBF4/propylene carbonate electrolytes. *ACS Energy Letters* **4,** 2843–2849 (2019).